

9.6 GHz and 34 GHz electron paramagnetic resonance studies of chromium-doped forsterite

David E. Budil,^{a)} Dong Gon Park,^{b)} and James M. Burlitch
Department of Chemistry, Cornell University, Ithaca, New York 14853

Roland F. Geray and Rüdiger Dieckmann
Department of Materials Science and Engineering, Cornell University, Ithaca, New York 14853

Jack H. Freed^{c)}
Department of Chemistry, Cornell University, Ithaca, New York 14853

(Received 25 January 1994; accepted 23 May 1994)

Chromium-doped forsterite single crystals grown under conditions that produce a high $\text{Cr}^{4+}/\text{Cr}^{3+}$ ratio were examined by electron paramagnetic resonance (EPR) at 9.6 and 34 GHz. The crystals were grown in 2–3 atm of oxygen by the floating-zone method starting from polycrystalline chromium-doped forsterite powder synthesized via a sol-gel method. Three crystals with chromium concentrations of 110, 300, and 390 ppm were studied. At 34 GHz, transitions are observed for the laser-active tetrahedral Cr^{4+} species that are not observable at 9.6 GHz, which improve the resolution and accuracy with which the magnetic parameters can be measured by EPR. In addition, peaks for a non-Kramers species appear at 34 GHz that were not observed at 9.6 GHz. These peaks are not analyzed in detail, but are tentatively ascribed to Cr^{4+} in the octahedral substitution sites of the crystal. At the highest chromium concentration, the Cr^{3+} spectra show evidence of direct interaction with Cr^{4+} . A global least-squares fit of the combined 9.6 and 34 GHz data for the 300 ppm crystal gives $D=64.26\pm 0.18$ GHz, $E=-4.619\pm 0.009$ GHz, $g_x=1.955\pm 0.009$, $g_y=2.005\pm 0.040$, $g_z=1.965\pm 0.006$, and places the magnetic z axis in the ab plane at an angle of $43.8\pm 0.3^\circ$ from the b crystallographic axis (in P_{bnm}). A method for accurately measuring the $\text{Cr}^{4+}/\text{Cr}^{3+}$ ratio using EPR line intensities is given. The EPR linewidth of the Cr^{4+} center exhibits a strong orientation dependence that is well-modeled by including site variations in the D and E zero-field splittings and in the orientation of the z magnetic axis. The linewidth analysis reveals a high degree of correlation between the distributions in D and E , and a somewhat weaker correlation between E and the z axis orientation. These results are interpreted to suggest that the tetrahedral Cr^{4+} sites vary mainly in the degree of compression of the tetrahedral cage along the a crystallographic axis. The Cr^{4+} EPR linewidths increase significantly at higher chromium concentration, but maintain the same qualitative orientation dependence. The EPR data indicate that the major contribution to inhomogeneity in the tetrahedral site, which may be related to the tunable range of the Cr^{4+} laser center, is distortion induced by chromium substitution into the crystal lattice rather than direct chromium–chromium interactions.

I. INTRODUCTION

Chromium-doped forsterite ($\text{Cr}:\text{Mg}_2\text{SiO}_4$) is an optical lasing material with tunability at around $1.2\ \mu\text{m}$, a wavelength that is near optimal for use with fiber optical materials. The forsterite host crystal belongs to the orthorhombic P_{bnm} space group, and has three nonequivalent sites that may be occupied by dopant cations.¹ The chromium dopant can replace magnesium in either of two sites with pseudo-octahedral symmetry; $M1$, which has a mirror plane, and $M2$, which possesses inversion symmetry. In addition, chromium may substitute in the silicon site, which has pseudo-tetrahedral symmetry.

Since the tunable laser activity of $\text{Cr}:\text{forsterite}$ was first reported in 1988,² the material has been studied intensively.

Electron paramagnetic resonance (EPR) has proved to be a particularly valuable tool for characterizing the ground states of various paramagnetic dopant cations in forsterite, including Cr^{3+} ,^{3,4} Cr^{4+} (and possibly Cr^{2+}) (Refs. 5–9), and $\text{Cr}-\text{Al}$ centers,¹⁰ as well as Fe^{3+} ,^{11,12} Ni^{2+} ,¹³ and Mn^{2+} .¹⁴ Efforts to understand the physical origin of the tunability of $\text{Cr}:\text{forsterite}$ have raised questions about the identity of the active lasing ion and its occupation site within the host crystal. In particular, EPR studies of $\text{Cr}:\text{forsterite}$ have produced a variety of results that appear to reflect differences in the method of preparation. Most chromium-doped crystals have been prepared by the conventional Czochralski method, in which a reducing or inert atmosphere is needed to protect the crucible from oxidation.¹⁵ The reducing environment most likely produces a low $\text{Cr}^{4+}/\text{Cr}^{3+}$ ratio, which may account for the absence of any significant Cr^{4+} peaks in the earliest studies of Rager, in which Cr^{3+} occupying the $M1$ and $M2$ octahedral sites was characterized.^{3,4} More recently, crystals grown in oxidizing environments have yielded significant

^{a)}Present address: Department of Chemistry, Northeastern University, Boston, Massachusetts 02115.

^{b)}Present address: Department of Chemistry, Kansas State University, Manhattan, Kansas 66502.

^{c)}To whom correspondence should be addressed.

amounts of Cr^{4+} and permitted this species to be characterized as well.^{16,17}

At present, Cr^{4+} occupying the tetrahedral site is generally accepted as the lasing center. The most unambiguous evidence for this assignment comes from a comparison of field-dependent narrow-line fluorescence wavelengths with the EPR parameters of this site,^{6,7} and its close similarity with the EPR properties of the tetrahedral Cr^{4+} center in Åkermanite.^{8,18} However, the importance of other chromium species in the crystal for tunable laser activity remains unclear. Some recent studies have concluded that the presence of Cr^{3+} in the octahedral *M1* and *M2* sites adversely affects the laser performance. Other studies have suggested that interactions between Cr^{3+} and Cr^{4+} are needed for laser tunability.¹⁹

Given the good control over the concentration of the chromium dopant and the $\text{Cr}^{4+}/\text{Cr}^{3+}$ ratio afforded by the combination of sol-gel synthesis and the floating zone crystal growth method, it would be desirable to utilize EPR as a high-resolution analytical method for investigating the detailed effects of chromium substitution on the local site symmetry as well as on the nature of local site inhomogeneities that may be related to laser tunability. Unfortunately, conventional EPR near 9 GHz lacks resolution for the details that are of greatest relevance to the photophysics of the Cr^{4+} center. The major obstacle is that Cr^{4+} is a non-Kramers ion with a large *D* zero-field splitting parameter. Because of this, only one of the three possible spin state transitions is visible at frequencies near 9 GHz, where this center has been studied. This significantly limits the resolution available from EPR at conventional frequencies.

In addition, there remains the possibility that other occupation sites for Cr^{4+} exist (i.e., the octahedral sites) which may not be observable near 9 GHz owing to the large zero-field splittings expected for Cr^{4+} in this symmetry.²⁰ Although the identity of the lasing center is fairly clear at this point, the nature of its interactions with the crystal lattice as well as with nearby dopants in the *M1* and *M2* sites, and their effects on laser performance, has not been fully elucidated.

II. EXPERIMENTAL METHODS

A. Crystal growth

Single crystals of chromium-doped forsterite used in this study were grown in an oxygen atmosphere by the floating zone method. Single crystal growth starting from a mixture of metal oxides was unsuccessful because of incomplete reaction among the metal oxide particles due to slow diffusion and the volatility of chromium oxide at high temperatures. To overcome these problems, the feedstocks for single crystal growth were prepared from polycrystalline, chromium-doped forsterite powder synthesized by the sol-gel method.²¹ In this method, all the elements are homogeneously mixed at the molecular level, which eliminates the necessity of long-range diffusion. Briefly, the previously published sol-gel synthesis of pure forsterite²² was modified by introducing chromium as follows. After a solution of magnesium methoxide and tetraethylorthosilicate was par-

tially polymerized by controlled hydrolysis and condensation, chromium (II) acetate was introduced, and the polymerization was completed. The sol was dried into a xerogel, and heat-treated to calcine all the organic groups, and produce polycrystalline chromium-doped forsterite. Cylindrically shaped feedstocks with a length of 10 cm and diameter of 1 cm were prepared from the polycrystalline powder by pressing and subsequent sintering at 1300 °C in air. The feedstocks were melted by a focused beam in an elliptical mirror furnace without a crucible at 1900 °C, and single crystals were grown by controlled cooling of the melt under a stream of oxygen gas as described in detail elsewhere.²³ In order to enhance the ratio of Cr^{4+} to Cr^{3+} , the crystals were grown under 2–3 atm of oxygen instead of the 1 atm reported by Higuchi *et al.*²³

The single crystals appeared blue when viewed along the *a* crystallographic axis, and violet when viewed along each of the other two axes. The colors differed appreciably from the greenish-blue color (from Cr^{3+}) of crystals grown under a reducing atmosphere, suggesting that the $\text{Cr}^{4+}/\text{Cr}^{3+}$ ratio is generally higher. The three crystals used for this study had chromium concentrations of 110, 300, and 390 ppm, as determined by electron microprobe wavelength dispersive spectroscopy (WDS) and inductively coupled plasma mass spectroscopy (ICP/MS) analysis. The crystals were oriented by real-time, x-ray Laue backscattering techniques, and were cut along the directions of the crystallographic axes into approximately cubic shapes. The final sizes of the samples were $5.0 \times 1.8 \times 1.2 \text{ mm}^3$, $2.5 \times 1.8 \times 1.5 \text{ mm}^3$, and $2.0 \times 1.5 \times 1.0 \text{ mm}^3$ for the lowest, intermediate, and highest chromium concentrations, respectively.

B. EPR spectroscopy

EPR experiments were performed using a Bruker ER-200 series spectrometer with either a Bruker ER-044 X-band bridge or a Bruker ER-053 Q-band bridge, using standard 100 kHz field modulation. The X-band measurements were made at 9.6 GHz utilizing a Varian rectangular TE103 optical transmission cavity, and those at Q-band using a Bruker cylindrical TE cavity. Most spectra were obtained at room temperature; when lower temperatures (down to -125 °C) were required, cold dry nitrogen gas was flowed over the sample.

The crystals were mounted using rubber cement or contact adhesive onto a quartz rod that had a flat surface ground onto it. For rotation about each of the crystallographic axes, the selected crystal axis was aligned with the rotation axis by eye. Small crystal alignment errors were resolvable in the experimental crystal rotation curves, which could be taken into account by the nonlinear least-squares fitting procedure used (see below). EPR spectra were measured for crystals with chromium contents of 110 ppm and 300 ppm as a function of rotation angle, rotating the field direction in the *ab*, *bc*, and *ca* planes at each of the two frequencies used. The field was swept from 0.15 to 12.0 kG for the 9.6 GHz spectra, and from 3.00 to 14.0 kG for the 34 GHz spectra; each sweep range was separately calibrated with a Bruker ER-035M NMR gaussmeter.

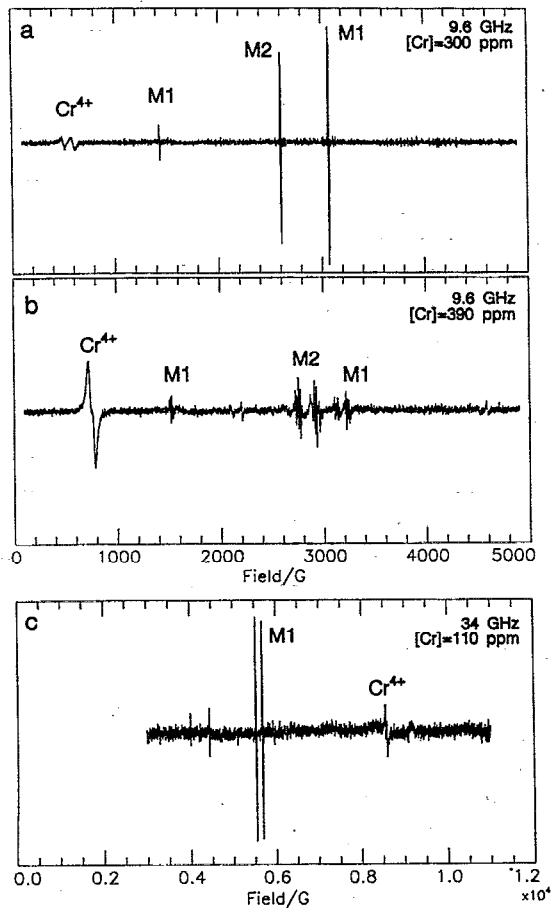


FIG. 1. Examples of EPR spectra of Cr:forsterite single crystals (a) $B_0 \parallel b$ at 9.6 GHz and 300 ppm chromium; (b) same orientation and frequency with 390 ppm chromium; (c) B_0 in ab plane at an angle of 43° from b , at 34 GHz and 110 ppm chromium. $M1$ and $M2$ identify peaks from octahedral Cr^{3+} .

III. RESULTS

For each of the crystals studied, several sets of EPR signals were observed both at 9.6 GHz and at 34 GHz. Representative spectra obtained at selected orientations, frequencies, and chromium concentrations are shown in Fig. 1. The major signals could be identified as the tetrahedral Cr^{4+} species that has been observed at X-band⁵⁻⁹ and the Cr^{3+} ions occupying the $M1$ and $M2$ octahedral sites, which have been thoroughly characterized by Rager and co-workers.^{3,4} Figure 1(b) illustrates one of the effects of high chromium concentration that was most immediately evident from the single-orientation EPR spectra. In the crystal with 390 ppm chromium, the main spectral lines of the Cr^{3+} exhibited a resolvable splitting, which most likely reflects electron spin-spin interactions between chromium centers at this concentration [cf. Fig. 1(b)]. However, because of the complicated pattern of overlapping peaks observed at most orientations of this crystal, a full analysis of the crystal rotation patterns was not undertaken for the present work. In addition to the peaks just mentioned, several peaks with significant intensity and linewidths comparable to those of the tetrahedral Cr^{4+} appeared in the 34 GHz spectra. Finally, several very minor,

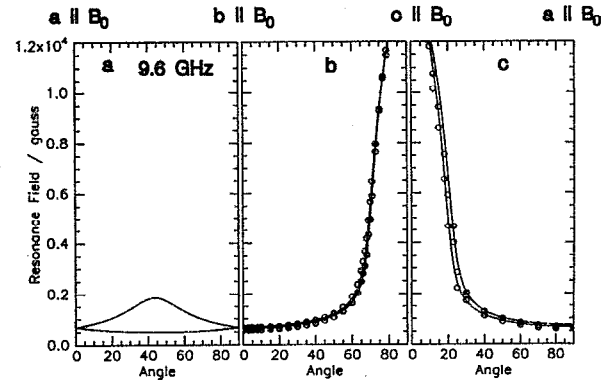


FIG. 2. Tetrahedral Cr^{4+} resonance field positions measured at 9.6 GHz as a function of single crystal orientation for rotation of B_0 in the (a) ab plane; (b) bc plane; and (c) ca plane. Lines represent nonlinear least-squares fit to the experimental data as described in the text. No peaks were experimentally observed in the ab rotation because of the small transition probability at these orientations.

narrow-lined signals were observed, one of which could be identified as Mn^{2+} from its distinctive six-line hyperfine pattern,¹⁴ but these were not analyzed in detail.

Figures 2 and 3 show combined results from the single crystal rotation studies of the tetrahedral Cr^{4+} center at both 9.6 and 34 GHz. The solid lines plotted in Figs. 2 and 3 are the calculated rotation patterns derived from the best-fit spin-Hamiltonian parameters as described in the next section. The crystals were mounted with a slight (2° or less) misalignment between the nominal axis of crystal rotation and the goniometer axis. This misorientation resulted in a doubling of the peaks for each rotation pattern of both Cr^{4+} (apparent in Figs. 2 and 3) and Cr^{3+} (data not shown). Each pair of peaks corresponds to sites that are related by C_2 symmetry about the nominal axis of crystal rotation. In order to obtain more accurate measurements of the Cr^{4+} linewidth (discussed be-

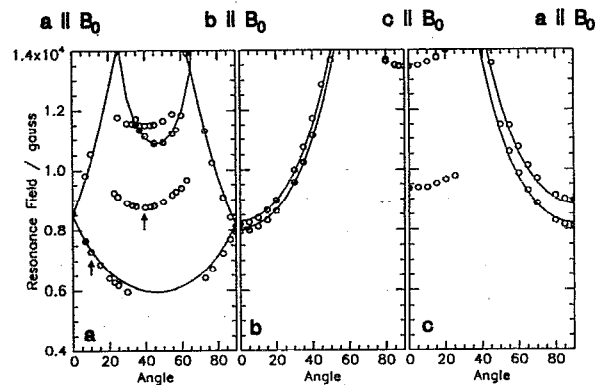


FIG. 3. Tetrahedral Cr^{4+} resonance field positions measured at 34 GHz as a function of single crystal orientation for rotation of B_0 in the (a) ab plane; (b) bc plane; and (c) ca plane. Lines represent nonlinear least-squares fits to the experimental data as described in the text. Peaks without lines correspond to additional strong peaks observed that could not be assigned to tetrahedral Cr^{4+} or octahedral Cr^{3+} ; arrows indicate orientations of spectra shown in Fig. 4.

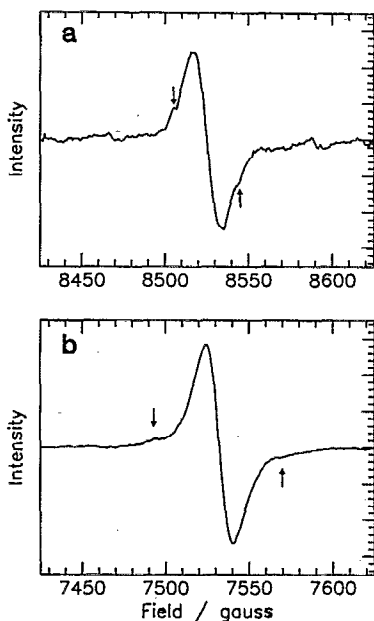


FIG. 4. Individual 34 GHz EPR spectra obtained for different orientations of B_0 in the ab plane [indicated by arrows in Fig. 3(a)]. (a) one of the broad, unassigned peaks described in the text, and (b) a peak from the tetrahedral Cr^{4+} center. Arrows indicate positions of minor side-peaks that may reflect hyperfine interaction with the 9% abundance ^{53}Cr nucleus ($I=3/2$).

low), no attempt was made to align the crystals further. Even very small misalignment angles would have resulted in an increase in the apparent Cr^{4+} linewidths due to unresolved peak doubling. Therefore, EPR measurements and subsequent analysis were carried out on the resolved pairs of peaks for each rotation pattern.

At 34 GHz, signals appeared that do not correspond to any previously reported chromium species, as shown by the symbols without an accompanying curve in Fig. 3. In Fig. 4, the spectrum of one of these peaks is compared with that from a peak assigned to the tetrahedral Cr^{4+} species; these two spectra were taken at the orientations indicated by the arrows in the Fig. 3. As can be seen from Fig. 4 the peaks from the two species are quite comparable; both are rather broad, with linewidths on the order of 20 G. Careful small-angle rotation studies of both peaks with slow field scans were conducted in an effort to isolate the peaks from any background interference and resolve any observable nuclear hyperfine splittings. For both tetrahedral Cr^{4+} and the unidentified species, two small shoulders were observed that tracked with the major peaks, shown by the arrows in Fig. 4. In both cases, however, the four hyperfine peaks expected for the ^{53}Cr isotope ($I=3/2$), which is present at approximately 9% natural abundance, could not be observed.

The tetrahedral Cr^{4+} peaks have a nearly Gaussian line shape at most of the orientations sampled at 9.6 GHz, with some distortions in the wings of the peaks. The distortion was most pronounced at the very lowest fields in the bc and ca rotations, where the peaks appeared skewed to the lower field side. In general, the line shapes observed at 34 GHz were quite Gaussian, excepting the very broad (ΔB_{pp}) > 160 G) peaks near 11 kG in the ab rotation [middle curve, Fig.

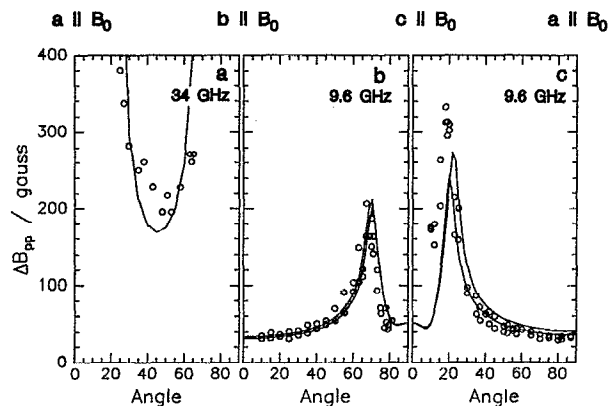


FIG. 5. Derivative peak-to-peak linewidths of selected tetrahedral Cr^{4+} lines as a function of rotation angle. (a) High field transitions in the ab rotation at 34 GHz, (b) and (c) low field transitions in the bc and ca rotations at 9.6 GHz, respectively. Lines indicate theoretical orientation dependence of the linewidths calculated using the statistical model described in the text. The two peaks in the low-field rotations result from the slight crystal misalignment discussed in the text.

3(a)]. Because of their weak intensity, these peaks suffered interference from background peaks (mostly Mn^{2+}) in the $g=2$ region, preventing an accurate determination of their true shapes and widths.

A striking orientation dependence for the linewidths of the Cr^{4+} peaks was observed for the samples containing 110 and 300 ppm chromium, which is shown in Fig. 5 for the 300 ppm crystal. The linewidths were determined by nonlinear least-squares fitting²⁴ of a Gaussian line shape function to the lines observed at 9.6 GHz in the bc and ca rotations. Because of the interference from background peaks, the linewidth of the higher-field transition in the ab rotation at 34 GHz could not be measured in this manner. Instead, the linewidths were determined by measurement of the derivative peak-to-peak distances directly from the spectra.

In the bc rotation at 9.6 GHz [Fig. 5(b)], the peak-to-peak derivative linewidth starts at about 40 G when $B_0 \parallel b$, and grows as the resonance field increases with increasing rotation angle. At an angle of approximately 70° , the linewidth goes through a maximum and decreases dramatically, although the resonance field continues to increase with rotation angle. This effect results from a "level crossing" between the two upper spin sublevels at this particular orientation; it was not possible to observe this effect in the 34 GHz bc rotation because the rotation curves could not be followed to sufficiently high field. The peaks observed in the bc and ca rotations at 34 GHz were significantly narrower than those observed at 9.6 GHz.

The Cr^{4+} linewidth was also observed to depend upon chromium content, as shown in Fig. 6. This figure compares the linewidths obtained for the bc rotation at chromium concentrations of 110 and 300 ppm; the lower-field of the two peaks produced by crystal misalignment have been omitted for clarity. The same qualitative orientation dependence is evident in both crystals; however, the linewidths measured at the lower chromium concentration are consistently smaller. The lines shown in Figs. 5 and 6 were calculated using a

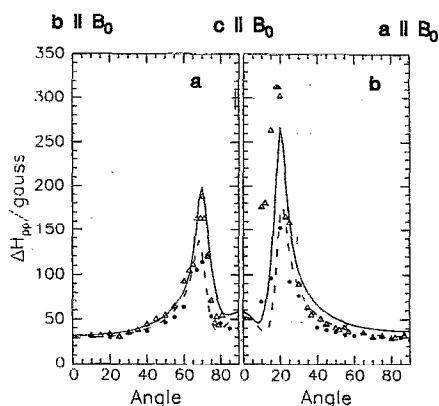


FIG. 6. Dependence of tetrahedral Cr^{4+} EPR linewidths on chromium concentration. Linewidths were measured at 9.6 GHz for rotation of B_0 in (a) the bc plane and (b) the ca plane and for chromium concentrations of (Δ) 300 ppm and (\bullet) 110 ppm. For clarity, only the widths of the lower-field of the pair of peaks produced by crystal misalignment are plotted.

simple statistical analysis assuming Gaussian distributions in the magnetic parameters of the Cr^{4+} center, as discussed in detail below.

The positions of the lower-field peaks assigned to the tetrahedral Cr^{4+} site (i.e., those peaks observed at orientations near $B_0 \parallel b$ and $B_0 \parallel a$) were observed to shift to higher field with decreasing temperature, as has been previously reported.^{7,8} The resonance field of the low-field peak measured at 9.6 and 34 GHz for $B_0 \parallel b$ is shown as a function of temperature in Fig. 7; the peaks at both frequencies shift by approximately +60 G upon going from 25 °C to -125 °C.

IV. ANALYSIS OF RESULTS

A. Analysis of single crystal rotation curves

All of the measured field vs rotation angle curves were analyzed using a modified Levenberg–Marquardt nonlinear least-squares algorithm²⁵ based on calculations using the spin Hamiltonian

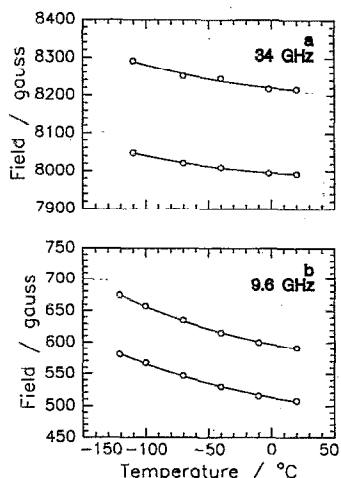


FIG. 7. Temperature dependence of the peak positions of the two low-field transitions of tetrahedral Cr^{4+} measured at (a) 34 GHz and (b) 9.6 GHz with $B_0 \parallel b$ and 300 ppm chromium. The two peaks in at each orientation result from the slight crystal misalignment discussed in the text.

$$H = \beta_e \mathbf{S} \cdot \mathbf{g} \cdot \mathbf{B}_0 + D(S_z^2 - \frac{1}{3}S^2) + E(S_x^2 - S_y^2), \quad (1)$$

and an effective electronic spin $S = \frac{3}{2}$ (for Cr^{3+}) or $S = 1$ (for Cr^{4+}). Peak positions were calculated from the spin Hamiltonian matrix using the eigenfield method described by Belford *et al.*²⁶

Before any attempt was made to analyze the results for tetrahedral Cr^{4+} , the well-characterized Cr^{3+} dopant was used as an internal standard for measuring the crystal misalignment angles accurately. The misalignment angles are defined as follows: first, the crystal is rotated through a “facial misalignment” angle η about the field direction, followed by a “lateral alignment” angle ς about the axis that is perpendicular to both the field and goniometer axis. (The third possible misalignment angle corresponds to an error in the zero of the goniometer rotation, which could be determined by inspection of the crystal rotation patterns.) Since the principal magnetic axes of Cr^{3+} in the $M2$ octahedral site lie nearly along the unit cell axes, this species did not exhibit any resolvable doubling of the resonance peaks with misorientation, and was not used in the following analysis.

The experimental peak positions of the Cr^{3+} in the $M1$ octahedral site were fitted by a nonlinear least-squares procedure using the magnetic parameters and principal axis orientations that have been previously measured by Rager,³ and varying only the misalignment angles η and ς defined above. Allowing the magnetic parameters of the Cr^{3+} ($M1$) to vary did not significantly affect the misalignment angles obtained by this method, although it did yield D and E values slightly different from those reported by Rager. The procedure was carried out for the ab , bc , and ca crystal rotations at both 9.6 and 34 GHz. The misalignment angles determined in this manner were then set at fixed values for the subsequent analysis of the Cr^{4+} rotation patterns.

The combined 9.6 and 34 GHz data shown in Figs. 2 and 3 were fit globally by varying the spin Hamiltonian parameters $|D|$, $|E|$, g_x , g_y , and g_z , and the Euler angles α , β , and γ (defined using the convention given by Zare²⁷) that specify the orientation of the magnetic axes x , y , and z relative to crystallographic a , b , and c . The results of the least-squares analysis, including the misalignment angles determined from the Cr^{3+} data, are given in Table I for the crystal containing 300 ppm chromium. The uncertainties reported for each parameter in Table I were obtained from the formal covariance matrix of the least-squares fit, assuming normally distributed errors in the experimental data. It should be noted that the Euler angles given in Table I correspond to the magnetic axis labeling convention used by Hoffman *et al.*⁶ in which the axis constrained to lie along crystallographic c is defined as magnetic x . This convention also defines E to be negative, given the result $D > 0$ from temperature studies of the EPR intensities.⁶ The simulations shown in Figs. 2 and 3 therefore assumed $D > 0$ and $E < 0$, although these signs were not determined from the rotation data.

B. Orientation dependence of Cr^{4+} linewidths

The orientation dependence of the tetrahedral Cr^{4+} linewidths shown in Fig. 5 is amenable to a simple statistical analysis that reproduces the observed rotation curves reason-

TABLE I. Magnetic parameters of the tetrahedral Cr^{4+} center in a Cr:forsterite crystal containing 300 ppm chromium and a $\text{Cr}^{4+}/\text{Cr}^{3+}$ ratio of 14.5. Parameters were determined from a global nonlinear least-squares fit to resonance field vs angle EPR data measured at 9.6 and 34 GHz and ambient temperature.

		Crystal misalignment angles		
		<i>ab</i> rotation	<i>bc</i> rotation	<i>ca</i> rotation
34 GHz	η	1.8°	0.6°	2.2°
	ς	1.4°	-0.9°	-0.5°
9.6 GHz	η	1.7°	0.6°	3.4°
	ς	-1.2°	2.7°	-0.1°
Magnetic parameters				
Euler angles of magnetic axes (<i>x,y,z</i>) in (<i>a,b,c</i>) frame				
α		46.2±0.3°		
β		90.0±0.2°		
γ		0.0±0.2°		
Principal <i>g</i> -values				
g_{xx}		2.005±0.040		
g_{yy}		1.955±0.009		
g_{zz}		1.965±0.006		
Zero-field splittings				
$ D $		64.26±0.18 GHz		
$ E $		4.619±0.009GHz		

TABLE II. Variances and covariances for site distributions in the *D* and *E* zero-field splittings and the α Euler angle specifying the orientation of the *z* magnetic axis of the tetrahedral Cr^{4+} site in Cr:forsterite at two different chromium concentrations.

[Cr] (ppm)	110	300
C_{DD} (GHz ²)	3.2×10^{-2}	5.3×10^{-2}
C_{EE} (GHz ²)	7.8×10^{-5}	9.9×10^{-5}
$C_{\alpha\alpha}$ (deg ²)	3.4×10^{-4}	1.8×10^{-3}
C_{DE} (GHz ²)	-2.6×10^{-3}	-2.3×10^{-3}
$C_{D\alpha}$ (GHz deg)	...	-1.0×10^{-3}
$C_{E\alpha}$ (GHz deg)	8.9×10^{-5}	9.9×10^{-5}

namely that they must be symmetric ($C_{jk} = C_{kj}$) and positive definite ($C_{jj} > 0; C_{jk} \leq [C_{jj}C_{kk}]^{1/2}$). To accommodate these restrictions, the C_{jk} coefficients were determined by a Levenberg–Marquardt nonlinear least-squares algorithm combined with a penalty function to enforce the appropriate constraints.

The partial derivative functions with respect to the *g*-tensor parameters were negligible compared to those with respect to the Euler angles and the *D* and *E* zero-field splittings, as might be expected from the predominance of zero-field interactions at the magnetic fields used in this work. Site variations in *g*-values were consequently dropped from consideration. Further simplification resulted from the fact that the magnetic *x* axis is constrained by symmetry to lie along the *c* crystallographic axis, so that variation in the β and γ angles could also be neglected. Thus, the linewidth analysis included only statistical distributions in *D*, *E*, and the α Euler angle, which determines the orientation of the magnetic *z* axis in the *bc* crystallographic plane. This reduced parameter set required the determination of only three variances, C_{DD} , C_{EE} , and $C_{\alpha\alpha}$, and three covariances C_{DE} , $C_{D\alpha}$, and $C_{E\alpha}$.

An initial estimate of each of these parameters was required for the nonlinear least-squares procedure. The initial values of the covariances were taken to be zero. Reasonable estimates of the variances C_{DD} , C_{EE} , and $C_{\alpha\alpha}$ were obtained by scaling the appropriate partial derivative function to match selected regions of the experimental rotation curves in which the peak position depends predominantly on only one magnetic parameter. Specifically, C_{DD} was estimated from the linewidth at the minimum in the high-field curve in the 34 GHz *ab* rotation [Fig. 3(a)], C_{EE} from the linewidths measured in the flat low-field part of the rotation patterns in the *bc* and *ca* rotations obtained at 9.6 GHz, and $C_{\alpha\alpha}$ from the average of the maxima in the linewidth curves in the 9.6 GHz *bc* and *ca* rotations.

The variances and covariances determined by the constrained nonlinear least-squares procedure are given in Table II for the crystals containing 110 and 300 ppm chromium. For the 110 ppm chromium crystal, the variances in *D* and *E* correspond to standard deviations of 0.18 GHz and 0.0088 GHz, or approximately 0.28% and 0.19%, respectively. At 300 ppm chromium, the standard deviations of *D* and *E* are, respectively, 0.23 GHz and 0.0099 GHz, or approximately 0.36% and 0.21%. The standard deviations in the α Euler

ably well. Given that the experimental peaks have approximately a Gaussian line shape, the linewidth may be expressed as a statistical distribution of resonance fields such that the variance σ^2 in the resonance field is equal to $\frac{1}{4}\Delta B_{pp}^2$, where ΔB_{pp} is the first derivative peak-to-peak width of the line. If the dominant contributions to σ^2 are from site variation in the spin Hamiltonian parameters, and if the parameters also have normal statistical (i.e., Gaussian) distributions, then the variance of each resonant field position, B_i , may be expressed in terms of the partial derivatives of B_i with respect to each of the variable parameters x_j ,²⁸

$$\sigma_{B_i}^2 = \sum_{j,k} C_{jk} \left(\frac{\partial B_i}{\partial x_j} \right) \left(\frac{\partial B_i}{\partial x_k} \right). \quad (2)$$

The matrix of coefficients C_{jk} is simply the covariance matrix for the parameters $\{x_j\}$, so that C_{jj} is the variance of the parameter x_j and C_{jk} is the covariance between the distributions in x_j and x_k .

In order to determine the *C* matrix for a given set of variables from the experimentally measured $\sigma_{B_i}^2$, it is first necessary to obtain the partial derivatives of the field position of each resonance peak with respect to each of the variable parameters. Partial derivative functions were calculated using a forward-differences approximation starting from the parameter values given in Table I (and the signs for *D* and *E* noted above) by introducing a relative step of 10^{-4} in each parameter. From Eq. (2) it is clear that the linewidth is a simple linear combination of the squares and cross-products of the numerically estimated partial derivative functions. In principle, the coefficients C_{jk} may be determined directly by a linear least-squares fit to a set of experimental $\sigma_{B_i}^2$ values; however, in practice, the solution is complicated by constraints arising from the properties of covariance matrices,

angle for the crystals containing 110 and 300 ppm chromium are 0.02° and 0.04° .

A very significant feature of the data that is reasonably well reproduced by this analysis is the marked asymmetry between the *bc* and the *ca* rotation curves at both 110 and 300 ppm chromium (cf. Figs. 5 and 6). Some difference between these two rotation curves might be expected as a result of the slight displacement of the *z* magnetic axis towards the *b* crystallographic axis (cf. Table I and Discussion below). The calculated derivative functions, particularly $(\partial B_i/\partial D)^2$ and $(\partial B_i/\partial \alpha)^2$, did exhibit very small differences between the *bc* and the *ca* rotations, but these differences could not account for the very pronounced asymmetry apparent in Figs. 5 and 6. In fact, the experimental results could only be reproduced with a significant covariance between α and the zero-field splitting parameters. Thus, the large difference in linewidths between the *bc* and the *ca* rotations at both 110 and 300 ppm chromium provides a clear experimental indication that there exists a high degree of correlation between the magnetic *z* axis orientation and the zero-field splittings.

C. EPR determination of relative site populations

Once the magnetic parameters and principal axes are known for Cr^{3+} and Cr^{4+} in each of the occupation sites in the crystal, the single-crystal EPR line intensities may be used to estimate the relative amounts of chromium in each oxidation state. However, before a comparison of line intensities from different species is possible, it is necessary to take into account the different spin state population distributions, spin-lattice relaxation times, and transition probabilities for each paramagnetic center, all of which will depend in general on temperature, orientation, or both.

For comparison with the Cr^{4+} signal, only the higher-field (i.e., $-\frac{1}{2} \rightarrow +\frac{1}{2}$) transitions of both the *M1* and *M2* octahedral Cr^{3+} sites were used. Two factors led to this choice. First, the $-\frac{1}{2} \rightarrow +\frac{1}{2}$ lines have significantly higher transition probabilities than the $-\frac{3}{2} \rightarrow +\frac{3}{2}$ transitions, giving intense signals that can be reliably integrated. Second, the $-\frac{3}{2} \rightarrow +\frac{3}{2}$ transitions for both the *M1* and the *M2* sites saturated at significantly lower microwave power than the $-\frac{1}{2} \rightarrow +\frac{1}{2}$ transitions. Thus, to avoid artifacts due to spin-lattice relaxation, the $-\frac{3}{2} \rightarrow +\frac{3}{2}$ lines were omitted from the analysis and the microwave power was attenuated by 20 dB relative to the point at which the maximal signal was observed for the $-\frac{1}{2} \rightarrow +\frac{1}{2}$ lines.

Figures 8(a), 8(b) and 8(c), 8(d) show the calculated ratios of the total peak intensities for the $\text{Cr}^{4+}/\text{Cr}^{3+}(\text{M1})$ and $\text{Cr}^{3+}(\text{M1})/\text{Cr}^{3+}(\text{M2})$ pairs, respectively. Here, "total peak intensity" for a given transition refers to the sum of intensities of that transition for all of the symmetry-related sites of a given species (i.e., if four different resonance fields are found for the transition at a given crystal orientation, the intensities of all four peaks are added together). The curves in Fig. 8 were obtained using the calculated transition probabilities and spin state population differences for each of the symmetry-related sites at each crystal orientation. Transition probabilities were calculated as described by Belford *et al.*,²⁶ and population differences were calculated utilizing a Boltzmann equilibrium distribution for the experimental tempera-

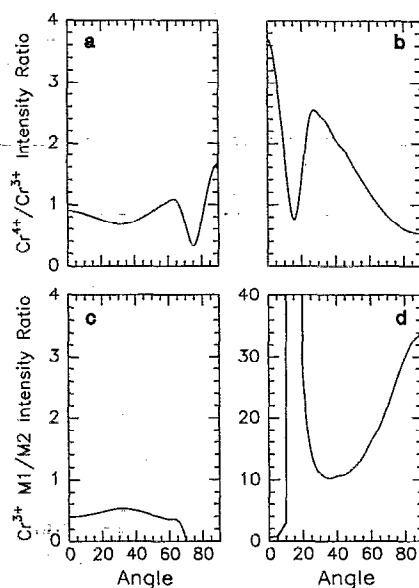


FIG. 8. Theoretical ratio of EPR peak intensity (peak volumes) for Cr^{4+} to $\text{Cr}^{3+}(\text{M1})$ as a function of B_0 orientation in the (a) *bc* plane; (b) *ca* plane and for $\text{Cr}^{3+}(\text{M1})/\text{Cr}^{3+}(\text{M2})$ as a function of B_0 orientation in the (c) *bc* plane and (d) *ca* plane, assuming equal populations of all three species. Only peaks corresponding to the $-\frac{1}{2} \rightarrow +\frac{1}{2}$ transitions are included for the Cr^{3+} species.

ture of 293 K, assuming that no excited electronic states of any center are significantly populated at this temperature. The signs of *D* that have been determined previously for each species^{3,6} were used in the calculation.

The peak intensity ratios shown in Fig. 8 were calculated for equal populations of Cr^{4+} , $\text{Cr}^{3+}(\text{M1})$, and $\text{Cr}^{3+}(\text{M2})$. Thus, the ratio of the populations of each pair of species in a given crystal may be determined by dividing the experimental ratio of integrated peak volumes for the pair at a selected orientation by the appropriate value plotted in Fig. 8. At the orientation with B_0 in the *ac* plane at an angle of 10° from the *a* axis, peaks from Cr^{3+} in the *M1* and *M2* octahedral sites, as well as the broad peaks from Cr^{4+} in the tetrahedral sites are present and well-separated in the 9.6 GHz spectrum. For the crystal containing 300 ppm of chromium, the doubly integrated peak volumes for the low-field Cr^{4+} transitions and the $-\frac{1}{2} \rightarrow +\frac{1}{2}$ transitions of both Cr^{3+} species gave relative populations of 0.93 ± 0.04 , 0.050 ± 0.002 , and 0.015 ± 0.002 for tetrahedral Cr^{4+} , octahedral $\text{Cr}^{3+}(\text{M1})$, and octahedral $\text{Cr}^{3+}(\text{M2})$, respectively.

V. DISCUSSION

A. Determination of Cr^{4+} magnetic parameters

As is evident in Figs. 2 and 3, the rotation patterns measured at 34 GHz reveal additional details of the tetrahedral Cr^{4+} site symmetry that are not resolvable at 9.6 GHz. Most significantly, whereas no transitions are observable at 9.6 GHz for the *ab* rotation because of their near-zero transition probability, three new curves appear at 34 GHz, which may be assigned to Cr^{4+} in the tetrahedral site. At the higher

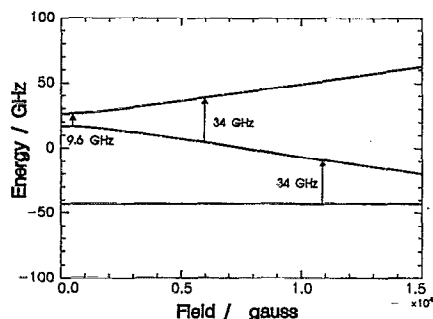


FIG. 9. Energy level diagram for the three Cr^{4+} spin sublevels as a function of field strength when $B_0 \parallel z$, illustrating the transitions observed at 9.6 GHz and at 34 GHz.

resonance fields corresponding to 34 GHz, the applied magnetic field mixes the zero-field states sufficiently to confer an appreciable probability onto the transitions.

The appearance of the middle curve in the 34 GHz ab rotation [Fig. 3(a)], with a minimum at about 10.9 kG, is particularly important because it permits the D zero-field splitting parameter to be directly and accurately measured by EPR. This can be seen from Fig. 9, which shows an energy level diagram illustrating the two transitions that occur at 34 GHz when B_0 is directed along the magnetic z axis and B_1 along magnetic x . This orientation corresponds to the rotation angle (about 47°) at the minima of the lower two curves in Fig. 3. At zero field, the spin sublevels are split into a doublet and a singlet separated by an energy D , with a splitting of $2E$ between the doublet levels. The peaks at lower field correspond to the transition between the upper two energy levels observed near 9 GHz, whereas the higher-field transitions occur between the lower two sublevels and thus span the major zero-field splitting D . Consequently, D can be obtained quite accurately from the 34 GHz data.

A second feature that is apparent in the 34 GHz ab rotation [Fig. 3(a)] is its asymmetry, for example, the lowest Cr^{4+} transition field for $B_0 \parallel a$ is somewhat higher than that for $B_0 \parallel b$ in this rotation. This effect cannot be due to the slight crystal misalignment present during the crystal rotation. In fact, alignment errors of 3° or less do not produce peak doubling or any resolvable shift of the resonance fields in the ab rotation, since the x principal magnetic axis of the Cr^{4+} is parallel (or nearly so) to the axis of crystal rotation. Thus, the asymmetry must reflect the orientation of the y and z principal magnetic axes of the Cr^{4+} . The asymmetry can also be seen in the inequivalence of the 34 GHz bc and ca rotations in Figs. 3(b) and 3(c). Although the crystal misalignments do produce peak doubling in these two rotation patterns, it is still evident that the curves representing the average position of each pair of peaks in the bc and ca rotations are not symmetric.

Our results therefore provide a slight refinement of previous EPR studies near 9 GHz, where the apparent equivalence of the bc and ca rotation curves [cf. Figs. 2(b) and 2(c)] would suggest that the z magnetic axis exactly bisects the a and b crystallographic axes. The results presented in Table I are closer to the fluorescence line narrowing measurement of

Hoffman *et al.*,⁶ which place the z magnetic axis somewhat closer to b . Although the difference between these two orientations is quite small (only about 1.2°), it still produces a significant asymmetry that is observable in the 34 GHz data. The influence of this small displacement has more profound implications in the interpretation of the orientation-dependent linewidths measured in the bc and ca rotations at 9.6 GHz, as discussed below.

It would be interesting to obtain a further EPR characterization of the tetrahedral Cr^{4+} center by determining the hyperfine tensor of the ^{53}Cr nucleus ($I = \frac{3}{2}$), as has been done for the Cr^{3+} dopant ions.⁴ Given the larger inhomogeneous linewidths of the Cr^{4+} species, accurate measurement of the orientation-dependent hyperfine splittings would require crystals doped with chromium enriched in ^{53}Cr .

B. Identification of the additional peaks at 34 GHz

Although no definitive identification of the additional peaks observed in the 34 GHz spectra (symbols without curves in Fig. 3) can be made at present, several observations suggest that these peaks may be attributable to some kind of Cr^{4+} species. First, the lines are significantly more intense than any of the other unassigned lines appearing in the spectra. Because of the carefully controlled conditions in the synthesis of the sol-gel precursor and the use of a crystal growth method that does not require a crucible, contaminants should be present in only very small quantities, suggesting that the extra peaks most likely correspond to the intended dopant cation. Furthermore, elemental analysis by ICP/MS shows that chromium is the only major dopant in the crystal, strongly supporting this suggestion. The appearance of hyperfine structure similar to that of tetrahedral Cr^{4+} (cf. Fig. 4) offers some additional corroboration for this conclusion. Finally, the linewidths of the additional peaks are significantly broader than any of the minor spectral lines. As discussed above, this feature is characteristic of a non-Kramers ion such as Cr^{4+} , for which the EPR linewidths directly reflect site variations in the zero-field parameters. In contrast, most of the major expected contaminants such as Mn^{2+} and Fe^{3+} are Kramers ions in which the linewidths are relatively unaffected by site variations.

These considerations are consistent with the alternative assignment of the extra lines to Cr^{2+} , however, this possibility is unlikely for two reasons. First, the crystal was grown in a highly oxidizing atmosphere, which should remove any Cr^{2+} that could have been present in the precursor sol-gel. Second, absorption spectra obtained from larger crystals grown under the same conditions as those used for EPR showed no absorption peaks characteristic of Cr^{2+} . These observations are consistent with the results of Yamaguchi *et al.*^{16,17} that no Cr^{2+} is observed when the crystal is grown at partial oxygen pressures above 0.01 atm, well below the pressures used in this work.

One difficulty with the assignment of the additional peaks to octahedral Cr^{4+} is that elementary crystal field theory²⁰ predicts an orbitally degenerate ground state (3T_1) for a d^2 ion in an octahedral field. Strong coupling between degenerate or near-degenerate states could lead to fast spin relaxation that obliterates the EPR signal at room tempera-

ture. Similar arguments apply to Cr^{2+} , a d^4 ion for which the ground state is orbitally degenerate in both octahedral and tetrahedral crystal fields. If Cr^{4+} (or Cr^{2+}) is present in the octahedral sites of the crystal, its crystal field would have to be highly distorted in order to remove the ground state degeneracy sufficiently to make it EPR-visible at higher temperatures. Alternatively, the additional signals may reflect a subpopulation of the tetrahedral Cr^{4+} species that is undergoing a strong electronic interaction with a neighboring dopant ion. In any case, it is clear that the extra peaks observed in this work do not correspond to the laser-active center. The zero-field splittings that have been determined from studies of the Zeeman effect on the narrow-line fluorescence wavelengths of the laser center^{8,18} are clearly inconsistent with the partial rotation curves shown in Fig. 3, whereas they are fully consistent with the EPR parameters determined for the tetrahedral Cr^{4+} .

C. Source of EPR line-broadening in Cr^{4+}

The nearly Gaussian shape of the Cr^{4+} EPR peaks provides a good indication that the linewidth arises from statistical variation among the chromium substitution sites. In principle, such variations can occur in any of the magnetic parameters of the Cr^{4+} center, including the orientations of the magnetic axes. One possibility that occurs very commonly in transition metals is site variation in the effective g -factor, or so-called “ g -strain.” However, as noted in the Results section, g -strain appears to be relatively unimportant in the present case, since the EPR linewidths are much less sensitive to variations in the g -values than to variations in the zero-field splittings and magnetic axis orientations. Unreasonably large distributions in the g -values would have been required to reproduce linewidths of the observed magnitude. These observations are consistent with the proximity of the principal g -values of the Cr^{4+} center to the free electron g -value; since the g -values of Cr^{4+} are not significantly influenced by the crystal field, they should be quite insensitive to small site variations within the crystal.

Another possible source of line broadening is interaction among the paramagnetic chromium substituents (including both Cr^{3+} and Cr^{4+}) in the crystal lattice. Indeed, as shown in Fig. 1(c), splittings attributable to spin–spin couplings do appear in the spectra of the $M1$ octahedral Cr^{3+} in the sample containing 390 ppm chromium. Because of the preponderance of Cr^{4+} in the sample, this splitting most likely arises from $\text{Cr}^{3+}/\text{Cr}^{4+}$ interactions. Splittings of this magnitude could therefore also be present in the Cr^{4+} peaks in this sample, but would be unresolvable because of the much larger linewidth of this species. Although linewidth contributions from spin–spin interactions cannot be ruled out, such contributions apparently constitute at most only a fraction of the overall Cr^{4+} linewidth, even at the highest chromium concentration studied.

The multiple peaks observed in the spectra from the $M1$ octahedral Cr^{3+} at the highest chromium concentration [cf. Fig. 1(c)] exhibit some unusual features that deserve some further comment. There was no evidence that these peaks arose from polycrystallinity in the sample; both x-ray Laue backscattering and polarizing microscopy showed a mon-

odomain crystal; nor was there any evidence of polycrystallinity in the other EPR signals. However the appearance of the splittings with higher chromium content is quite sudden, whereas there is no evidence of any spin–spin interactions at 300 ppm chromium, after an increase of only 30% in chromium content, the entire population of $M1$ octahedral Cr^{3+} exhibits the splittings [cf. Figs. 1(a) and 1(b)]. The appearance of a small number of distinct splittings also suggests a specific relative orientation of the species that is coupled to Cr^{3+} . If the occupation of nearby sites by other dopant ions were completely random, one would expect a gradual broadening of the peaks as the chromium concentration is increased, or at least the appearance of a large number of splittings. These observations suggest a cooperative substitution of specific chromium pairs in the crystal lattice at high chromium concentrations; however, further studies of the orientation-dependent splittings will be required to elucidate the nature of such pairs.

The analysis of the Cr^{4+} linewidth results clearly shows that the major source of the EPR linewidth variation are site distributions in D , E , and the z axis orientation. This interpretation is fully consistent with previous studies of EPR linewidths in non-Kramers ions.^{29,30} The best evidence for this conclusion is the very distinctive orientation dependence shown in Figs. 5 and 6, which cannot be reproduced by dipolar broadening mechanisms or by any combination of distributions in the g -values. Another good indication that g -strain and dipolar broadening can be neglected is the substantial narrowing of the peaks in the bc and ca rotations upon going from 9.6 to 34 GHz. Whereas spin–spin coupling should be frequency-independent, and g -strain should produce linewidths that increase at higher frequency, the linewidths of the peaks near the orientations $B_0 \parallel b$ and $B_0 \parallel c$ actually decreases from about 30 G at 9.6 GHz to less than 20 G at 34 GHz in the 300 ppm sample.

In sum, the results presented here suggest that the inhomogeneity observed in the EPR transitions of Cr^{4+} are dominated by site variations in the crystal field, rather than from direct chromium–chromium interactions. By analogy, the results presented here also imply that the optical transition linewidths of the Cr^{4+} center, which determine the tunability of its laser activity, could be more significantly influenced by site inhomogeneity than by chromium–chromium interactions. Since the EPR linewidths increase with increasing chromium concentration, it appears that the site inhomogeneities result from distortions induced by chromium substitution into the crystal lattice. In fact, preliminary results from this laboratory³¹ suggest a more specific effect. In a crystal grown under a reducing atmosphere to produce a low $\text{Cr}^{4+}:\text{Cr}^{3+}$ ratio (0.02:0.98 as measured by EPR), the experimental Cr^{4+} linewidths are approximately 3 G for $B_0 \parallel a$ and $B_0 \parallel b$ (data not shown). These linewidths are quite narrow compared to those observed for Cr^{4+} at the same crystal orientations in the present study (over 30 G, cf. Figs. 5 and 6). This apparent reduction in the tetrahedral site inhomogeneity at a low $\text{Cr}^{4+}:\text{Cr}^{3+}$ ratio suggests that the lattice distortions arise specifically from Cr^{4+} substitution at the tetrahedral site.

Presumably the inhomogeneity that is evident in the tet-

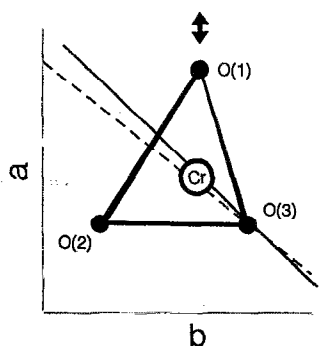


FIG. 10. Projection of the experimentally determined magnetic z axis (solid line) onto the tetrahedral cage occupied by Cr^{4+} in the forsterite crystal, as viewed along the c crystallographic axis. Dashed line indicates the orientation of the line connecting the midpoints of opposite sides of the tetrahedron. Arrow indicates likely direction of cage distortion that produces site variation at the Cr^{4+} , as discussed in the text.

rahedral site of forsterite is also present in the adjacent octahedral sites. X-ray crystallography of a series of olivines has revealed significant distortion in the crystal lattice as the fraction of iron substituted into the octahedral sites of the forsterite host increases, particularly for the $M1$ site.¹ However, even if the Cr^{3+} dopants do undergo site variation in D and E , the widths of their EPR peaks will be affected to a much smaller degree than those of Cr^{4+} , since the transitions occur between Kramers doublets in the case of Cr^{3+} .

D. Geometric interpretation of EPR results

A comparison of the experimental zero-field axes with the atomic coordinates of the tetrahedral cage¹ enclosing the Cr^{4+} yields some insights into the nature of the local crystal field of the lasing center. The major zero-field axis, z , is expected to adopt an orientation that depends upon the symmetry of the dominant type of distortion in the tetrahedron. For trigonal (C_{3v}) distortions in which one of the Cr–O distances is altered, z might be expected to lie along the axis of the altered bond, which becomes an axis of threefold symmetry. Alternatively, if the dominant distortion is tetragonal (C_{2v}), corresponding to elongation or compression along an axis connecting opposite edges of the tetrahedron, z should again be aligned with the symmetry axis. The crystal structure of forsterite suggests the first of these possibilities, since the Si–O(1) bond along crystallographic a is appreciably shorter than the other Si–O bonds in the tetrahedron. However, the measured zero-field axes are more consistent with the latter type of distortion. Figure 10 depicts the experimentally determined z axis (solid line) relative to the Cr^{4+} tetrahedron as viewed along the c crystallographic axis. The dashed line shows the direction of the axis connecting the midpoints of the $O(3)$ – $O(3)'$ and $O(1)$ – $O(2)$ edges of the tetrahedron (using the notation of Birle *et al.*¹), which lies in the ab plane at an angle of 38° from b . It should be noted that this direction was derived from atomic coordinates for the SiO_4 tetrahedron, which may not be strictly comparable to the chromium-substituted tetrahedron. Nevertheless, the main conclusion from Fig. 10 is that the dominant type of

distortion is neither purely trigonal or tetragonal, but probably represents an asymmetric elongation of the tetrahedron approximately along z .

The correlations between the distributions in D , E , and α may also be interpreted in terms of a simplified geometric model for distortions in the local crystal field of Cr^{4+} . Specifically, the large negative covariance C_{DE} found for both 110 and 300 ppm chromium give correlation coefficients of -0.95 and -0.96 , respectively, indicating that the distributions in the zero-field splitting parameters are strongly correlated in both samples. More specifically, higher D values are correlated with more negative E values, i.e., larger $|E|$. The covariance $C_{E\alpha}$ is also significant at both concentrations, yielding correlation coefficients of 0.55 and 0.45 for 110 and 300 ppm, respectively. Thus, more positive E values (smaller $|E|$) tend to be correlated with larger α values, i.e., a smaller angle between magnetic z and crystallographic b . In combination, these results suggest a picture in which compression of the tetrahedral cage along crystallographic a (cf. Fig. 10) leads to (i) a displacement of z towards b ; (ii) a reduction in D due to the increased strength of the crystal field; and (iii) a partial restoration of axial symmetry, reflected in a reduction of $|E|$.

This model is consistent with the observed temperature dependence of the low-field peak positions of Cr^{4+} near $B_0 \parallel b$ (cf. Fig. 7). The shift in resonance field with temperature must be due almost entirely to changes in $|E|$, since the resonance field at this orientation is insensitive to the g -values and nearly independent of D . The fact that similar peak shifts are observed for $B_0 \parallel b$ and $B_0 \parallel a$ rules out the possibility of any rotation of the z magnetic axis in the ab plane with decreasing temperature. Thus, the increase of approximately $+60$ G in resonance field corresponds to a decrease in $|E|$ of about 0.17 GHz upon going from 25°C to -125°C . According to the correlations inferred from the linewidth data, a smaller $|E|$ reflects a more compressed and axially symmetric tetrahedron, consistent with the notion that the tetrahedral cage of the Cr^{4+} ion is simply contracting slightly at lower temperatures. These temperature-dependent changes in the crystal field of Cr^{4+} , although small, may still significantly affect the laser performance of Cr:forsterite at lower temperatures.

VI. CONCLUSION

EPR spectroscopy at 9.6 and 34 GHz has been applied to chromium-doped forsterite in conjunction with a strategy of precursor synthesis and crystal growth that affords good control over the concentration and $\text{Cr}^{4+}/\text{Cr}^{3+}$ ratio of the chromium dopant ions. Three single crystals were studied with chromium contents of 110, 300, and 390 ppm, respectively.

At 34 GHz, Cr^{4+} transitions appear that are unobservable at the more conventional frequency of 9.6 GHz. The additional information available at 34 GHz improves the accuracy with which the zero-field splittings and the directions of the zero-field magnetic axes of the tetrahedral Cr^{4+} center may be determined. Specifically, a global least-squares fit of the combined 9.6 and 34 GHz data for the 300 ppm crystal gave $g_x = 1.955 \pm 0.009$, $g_y = 2.005 \pm 0.040$, $g_z = 1.965$

± 0.006 , $D = 64.26 \pm 0.18$ GHz, $E = -4.619 \pm 0.009$ GHz, and an orientation for the magnetic z axis in the ab plane at an angle of $43.8 \pm 0.3^\circ$ from b .

Significant changes appear in the EPR properties of the tetrahedral Cr^{4+} center as a function of chromium concentration and temperature. The EPR linewidth is strongly orientation-dependent, which was attributed to site variation of the D and E zero field splittings and the orientation of the z magnetic axis. The distributions in these parameters all increase with increasing chromium concentration, indicating that the inhomogeneity in the tetrahedral site arises from distortions induced by chromium substitution into the crystal lattice, rather than from direct chromium–chromium interactions. The significant correlations among the distributions in D , E , and z axis orientation were interpreted in terms of a simple geometric model in which the tetrahedral cage of the Cr^{4+} ion is compressed by a variable degree along the a crystallographic axis. The correlations inferred from the linewidth data are also consistent with the observed reduction in $|E|$ at lower temperatures.

An EPR method was presented for determining the $\text{Cr}^{4+}/\text{Cr}^{3+}$ ratio and fractional occupation of each of the chromium substitution sites in forsterite based on the known magnetic parameters of the different chromium species. For the 300 ppm crystal, the method gave relative populations of 0.94, 0.050, and 0.015 for tetrahedral Cr^{4+} , octahedral $\text{Cr}^{3+}(M1)$, and octahedral $\text{Cr}^{3+}(M2)$, respectively.

Taken together, the results presented here demonstrate the sensitivity of EPR to a variety of factors that are directly under synthetic control, and which report at least indirectly on the optical properties of the Cr^{4+} center. Thus, EPR promises to be a useful analytical tool for guiding synthetic strategies towards improving the laser performance of Cr: forsterite. Future studies in this laboratory will be directed towards establishing a more direct correspondence between the observable magnetic and optical properties of the Cr^{4+} center. Particularly promising will be combinations of EPR with optical methods, such as ODMR, which will allow one to relate site inhomogeneities observable by EPR directly to the optical properties of the sample.

ACKNOWLEDGMENTS

This work was supported by the MRL program of the NSF under Award No. DMR-9121654 and by NSF Grant No. CHE-9312167. We thank Jennifer Mass for providing unpublished EPR results from Cr:forsterite grown in a reducing atmosphere. Computations were performed at the Cornell National Supercomputer Facility (CNSF) and at the computer facilities of the Cornell Materials Science Center.

- ¹J. D. Birle, G. V. Gibbs, P. B. Moore, and J. V. Smith, *Am. Miner.* **53**, 807 (1968).
- ²V. Petricevic, S. K. Gayen, R. R. Alfano, K. Yamagishi, M. Anzai, and Y. Yamaguchi, *Appl. Phys. Lett.* **52**, 1040 (1988).
- ³H. Rager, *Phys. Chem. Miner.* **1**, 371 (1977).
- ⁴H. Rager, *Z. Naturforsch.* **35a**, 1296 (1980).
- ⁵J. Casa-Gonzales, S. M. Jacobsen, K. R. Hoffman, and W. M. Yen, in *OSA Proceedings on Advanced Solid-State Lasers*, edited by G. Dube and L. Chase (Optical Society of America, Washington, DC, 1991), Vol. 10, pp. 64–68.
- ⁶K. R. Hoffman, J. Casa-Gonzales, S. M. Jacobsen, and W. M. Yen, *Phys. Rev. B* **44**, 12 589 (1991).
- ⁷M. H. Garrett, V. H. Chan, H. P. Jenssen, M. H. Whitmore, A. Sacra, D. J. Singel, and D. J. Simkin, in *OSA Proceedings on Advanced Solid-State Lasers*, edited by A. Pinto and L. Chase (Optical Society of America, Washington, DC, 1992), Vol. 13, p. 17.
- ⁸M. H. Whitmore, A. Sacra, and D. J. Singel, *J. Chem. Phys.* **98**, 3656 (1993).
- ⁹V. G. Baryshevski, M. V. Korznik, M. G. Livshitz, A. A. Tarasov, A. E. Kimaev, I. Mishkel, M. L. Meilman, B. J. Minkov, and A. P. Shkadaravich, in *OSA Proceedings on Advanced Solid-State Lasers*, edited by G. Dube and L. Chase (Optical Society of America, Washington, DC, 1991), Vol. 10, pp. 26–34.
- ¹⁰S. Nagel and H. Rager, *Phys. Chem. Miner.* **12**, 291 (1985).
- ¹¹H. Rager, *J. Mol. Struct.* **58**, 215 (1980).
- ¹²J. M. Gaité and S. S. Hafner, *J. Chem. Phys.* **80**, 2747 (1988).
- ¹³H. Rager, S. Hosoya, and G. Weiser, *Phys. Chem. Miner.* **15**, 383 (1989).
- ¹⁴J. Michoulier, J.-M. Gaité, and B. Maffeo, *C. R. Acad. Sci. Ser. B* **269**, 535 (1969).
- ¹⁵H. Takei and T. Kobayashi, *J. Cryst. Growth* **23**, 121 (1974).
- ¹⁶Y. Yamaguchi, K. Yamagishi, and Y. Nobe, in *OSA Proceedings on Advanced Solid-State Lasers*, edited by G. Dube and L. Chase (Optical Society of America, Washington, DC, 1991), Vol. 10, pp. 52–56.
- ¹⁷Y. Yamaguchi, K. Yamagishi, and Y. Nobe, *J. Cryst. Growth* **128**, 996 (1993).
- ¹⁸T. S. Rose, R. A. Fields, M. H. Whitmore, and D. J. Singel, in *OSA Proceedings on Advanced Solid-State Lasers*, edited by G. Dube and L. Chase (Optical Society of America, Washington, DC, 1991), Vol. 10, pp. 64–68.
- ¹⁹H. R. Verdun and L. Merkle, in *OSA Proceedings on Advanced Solid-State Lasers*, edited by G. Dube and L. Chase (Optical Society of America, Washington, DC, 1991), Vol. 10, p. 35.
- ²⁰J. R. Pilbrow, *Transition Ion Electron Paramagnetic Resonance* (Clarendon, Oxford, 1990).
- ²¹D. G. Park, J. M. Burlitch, R. F. Geray, R. Dieckmann, D. B. Barber, and C. R. Pollock, *Chem. Mater.* **5**, 518 (1993).
- ²²J. M. Burlitch, M. L. Beeman, B. Riley, and D. L. Kohlstedt, *Chem. Mater.* **3**, 692 (1991).
- ²³M. Higuchi, R. F. Geray, R. Dieckmann, D. G. Park, J. M. Burlitch, D. B. Barber, and C. R. Pollock, *J. Cryst. Growth* (submitted).
- ²⁴GENPLOT program, Computer Graphic Service, Ltd., Ithaca, New York.
- ²⁵J. J. Moré, B. S. Garbow, and K. E. Hillstom, *Users' Guide for MINPACK-1*, publication ANL 80-74 (National Technical Information Service, Springfield, VA, 1980).
- ²⁶G. G. Belford, R. L. Belford, and J. F. Burkhalter, *J. Magn. Reson.* **11**, 251 (1973).
- ²⁷R. N. Zare, *Angular Momentum* (Wiley–Interscience, New York, 1988).
- ²⁸P. R. Bevington, *Data Reduction and Error Analysis for the Physical Sciences* (McGraw–Hill, New York, 1969).
- ²⁹C. M. Bowden, H. C. Meyer, and P. L. Donoho, *Phys. Rev. B* **3**, 645 (1971).
- ³⁰C. M. Bowden, H. C. Meyer, and P. L. Donoho, *Phys. Rev. B* **3**, 656 (1971).
- ³¹J. Mass, J. M. Burlitch, D. E. Budil, and J. H. Freed (unpublished results).